

In Vivo Evaluation of Corneal Biomechanics Following Cross-Linking Surgeries Using Optical Coherence Elastography in a Rabbit Model of Keratoconus

Yanzhi Zhao^{1,*}, Yirui Zhu^{2,3,*}, Yange Yan⁴, Hongwei Yang¹, Jingchao Liu⁵, Yongan Lu⁵, Yingjie Li⁵, and Guofu Huang¹

¹ Eye Center, Second Affiliated Hospital of Nanchang University, Nanchang, Jiangxi, China

² School of Physics, University of Nanjing, Nanjing, Jiangsu, China

³ School of Testing and Opto-electronic Engineering, Nanchang Hangkong University, Nanchang, Jiangxi, China

⁴ Yujiang District People's Hospital, Jiangxi, China

⁵ Department of Ophthalmology, Nanchang First Hospital, Nanchang, Jiangxi, China

Correspondence: Guofu Huang, Eye Center, Second Affiliated Hospital of Nanchang University, 1 Minde Road, Nanchang, Jiangxi 330000, China.

e-mail: hgf2222@sina.com

Yingjie Li, Department of Ophthalmology, Nanchang First Hospital, 128 Xiangshan Northern Road, Nanchang, Jiangxi 330009, China. e-mail: 422094465@qq.com

Received: July 8, 2023

Accepted: December 30, 2023

Published: February 20, 2024

Keywords: optical coherence elastography; optical coherence tomography; keratoconus biomechanics; corneal cross-linking surgery; ultrasmall ultrasound transducers

Citation: Zhao Y, Zhu Y, Yan Y, Yang H, Liu J, Lu Y, Li Y, Huang G. In vivo evaluation of corneal biomechanics following cross-linking surgeries using optical coherence elastography in a rabbit model of keratoconus. *Transl Vis Sci Technol.* 2024;13(2):15, <https://doi.org/10.1167/tvst.13.2.15>

Purpose: Validation of the feasibility of novel acoustic radiation force optical coherence elastography (ARF-OCE) for the evaluation of biomechanical enhancement of the in vivo model of keratoconus by clinical cross-linking (CXL) surgery.

Methods: Twelve in vivo rabbit corneas were randomly divided into two groups. Both groups were treated with collagenase type II, and a keratoconus model was obtained. Then, the two groups were treated with CXL procedures with different irradiation energy of 15 J and 30 J (CXL-15 J and CXL-30 J, respectively). An ARF-OCE probe with an ultrasmall ultrasound transducer was used to detect the biomechanical properties of cornea. An antisymmetric Lamb wave model was combined with the frequency dispersion relationship to achieve depth-resolved elastography.

Results: Compared with the phase velocity of the Lamb wave in healthy corneas (approximately 3.96 ± 0.27 m/s), the phase velocity of the Lamb wave was lower in the keratoconus region ($P < 0.05$), with an average value of 3.12 ± 0.12 m/s. Moreover, the corneal stiffness increased after CXL treatment ($P < 0.05$), and the average phase velocity of the Lamb wave was 4.3 ± 0.19 m/s and 4.54 ± 0.13 m/s after CXL-15 J and CXL-30 J treatment.

Conclusions: The Young's moduli of the keratoconus regions were significantly lower than the healthy corneas. Moreover, the Young's modulus of the keratoconus regions was significantly higher after CXL-30 J treatment than after CXL-15 J treatment. We demonstrated that the ARF-OCE technique has great potential in screening keratoconus and guiding clinical CXL treatment.

Translational Relevance: This work accelerates the clinical translation of OCE systems using ultrasmall ultrasound transducers and is used to guide CXL procedures.

Introduction

Keratoconus, a form of corneal ectasia, is a vision disorder that has been found clinically to damage

the cornea if left untreated. Moreover, in the most severe cases, the cornea may be perforated.^{1,2} Clinical histopathological studies have revealed three features in the pathogenesis of keratoconus: thinning of the corneal stroma, breakage in Bowman's layer, and iron

deposits in the basal layer of the corneal epithelium.^{3,4} The macroscopic morphological features of keratoconus are decreased corneal thickness and increased curvature in the onset area.^{5,6} Furthermore, keratoconus has different stromal distributions and less stroma than normal corneas, resulting in lower biomechanical strength and thinning in keratoconus, which represent important pathogenic features.⁷⁻⁹ Thus, the assessment of corneal biomechanics has become an important method for diagnosing keratoconus in clinical practice.

Corneal cross-linking (CXL), by increasing the stiffness of the cornea, is a common and effective clinical treatment for keratoconus.¹⁰ The standard CXL method is the Dresden protocol, which consists of 30 minutes of exposure to 3 mW fluence (5.4 mJ/cm²) followed by 30 minutes of soaking in 0.1% riboflavin.¹¹ Specifically, in the CXL procedure, the interaction between the photosensitizer riboflavin and ultraviolet A irradiation triggers a photochemical reaction to covalently cross-link collagen fibers, thereby increasing the stiffness of the cornea.¹² Therefore, the efficacy of the Dresden CXL protocol is thought to depend on changes in corneal biomechanical properties that are induced by altering the properties of collagen fibers within the cornea and intrafibrillar binding. Thus, evaluating corneal biomechanics is one of the most important methods to assess the efficacy of CXL.^{13,14}

Different commercial instruments have been developed, including the ocular response analyzer and the Corvis-ST, which both use the pressure generated by air pulses to assess the corneal biomechanics.^{15,16} The ocular response analyzer measures the corneal hysteresis and the corneal resistance factor.¹⁷ The corneal hysteresis and corneal resistance factor of corneas with forme fruste keratoconus are significantly lower than those of normal corneas; moreover, the corneal hysteresis and corneal resistance factor in both keratoconus and postoperative corneas are significantly lower than those of normal corneas and corneas after refractive procedures.¹⁸⁻²⁰ However, the clinical use of these parameters is limited by their low sensitivity and specificity; therefore, the reliability of the results requires further study.¹⁷ Several parameters can be measured by Corvis-ST, including the applanation velocity 2, the second applanation length, and so on. Previous studies have shown that the Corvis-ST has high sensitivity and specificity in differentiating normal and keratoconus by combining multiple parameters in a logistic regression equation. There are also reports of *in vivo* studies based on Corvis-ST demonstrating changes in the corneal biomechanics after CXL.^{21,22} Unfortunately, the existing parameter indices are not standardized and are

not linked to conventional physical parameters such as the Poisson's ratio and density, and they do not allow for quantitative evaluation of the biomechanical stiffness of the cornea, such as Young's modulus and shear modulus.²³ Therefore, *in vivo* quantitative corneal biomechanical property measuring techniques are urgently needed for clinical ophthalmic diagnosis and treatment.

Elastography is another emerging technique for evaluating the corneal biomechanics, including ultrasonic elastography, Brillouin microscopy, and optical coherence elastography (OCE).^{24,25} Qian et al.²⁶ used a confocal 40-MH needle ultrasound transducer to assess the corneal Young's modulus after formalin treatment at different IOPs. Weng et al.²⁷ used a high-frequency ultrasound array method for ultrafast ultrasound imaging and a Lamb wave model to assess the porcine cornea viscoelasticity. Zhang et al.^{28,29} used a mechanical shaker probe combined with high-frequency ultrasonic elastography to assess the biomechanics of the anterior ocular segment and whole eye tissue. However, given the fine arrangement of the five-layer corneal structure, ultrasonic elastography cannot achieve high-resolution micron-level detection *in vivo*. Brillouin microscopy allows direct calculation of the longitudinal moduli of biological tissues by measuring the spectral frequency shift of scattered light in the tissue.³⁰ Several articles have reported on the use of Brillouin microscopy to assess the effects of keratoconus, CXL surgery, and hydration on corneal biomechanical properties.³¹⁻³⁴

OCE is an elastography technique that was developed on the optical coherence tomography (OCT), with the advantages of high resolution, high signal-to-noise ratio, and three-dimensional (3D) imaging. Chen et al. proposed the ARF-OCE technique to quantify the elastic modulus of the cornea, lens, retina.³⁵⁻³⁷ Zvietcovich et al.³⁸ developed an OCE system with air-coupled ultrasound transducer excitation and observed increased corneal biomechanical properties after CXL surgery. Pitre et al.³⁹ proposed an OCE system incorporating air-coupled ultrasound examination to assess the biomechanics of anisotropic corneal tissue. De Stefano et al.⁴⁰ used the compression OCE technique to evaluate the biomechanical properties of healthy and keratoconus in human volunteers for the first time and found significant differences in biomechanical properties between healthy and keratoconus. In our previous study, the biomechanical properties of the keratoconus in isolated human eyes were evaluated using the OCE technique, and it was found that the corneal elastic modulus was decreased significantly for the conical region.⁴¹

Although these studies suggest that corneal biomechanical properties have the potential to be a biomarker for the clinical diagnosis of keratoconus, there is still a need for more detailed evaluation of changes in biomechanical properties of keratoconus during clinical interventions, such as CXL surgery, a widely used treatment.

In this work, we propose an ARF-OCE system incorporating an ultrasmall ultrasound transducer (USUT) to evaluate the biomechanics of an in vivo keratoconus model, and keratoconus after CXL treatments in vivo. We discuss the biomechanical properties of the in vivo keratoconus model and evaluate the changes in the biomechanical properties of the keratoconus regions during different CXL process. We believe that this research on the biomechanical properties of the keratoconus will accelerate the clinical translation of OCE.

Methods

Sample Preparation and Experimental Design

A total of six New Zealand White rabbits (aged 5–7 months, weighing 3.0–3.5 kg; a total of 12 corneas) were randomly divided into two groups of three rabbits and labelled as follows: group 1 (rabbit 1, rabbit 2, and rabbit 3) and group 2 (rabbit 4, rabbit 5, and rabbit 6). The untreated contralateral eyes of the rabbits in the first and second groups served as the control group. All surgeries and experiments were preceded by intramuscular injections of 35 mg/kg ketamine and 5 mg/kg xylazine to induce anesthesia. Before the OCE experiments, the corneal topography and intraocular pressure (IOP) were measured by a Pentacam HR (Ocular, Wetzlar, Germany) and rebound tonometer, respectively. During the OCE experiments, lactated Ringer's solution was used to maintain corneal surface wetness. All animal procedures were approved by the Animal Experimentation Ethics Committee of Nanchang Eye Hospital, Zhongshan Eye Center, Sun Yat-sen University, in accordance with the Declaration of Helsinki and ARVO.

In the first and second groups, the keratoconus model was obtained by applying type II collagenase treatment to healthy rabbit corneas.⁴² Type II collagenase was obtained as a powder dissolved in a balanced salt solution of 15% dextran at a proportional concentration of 5 mg/mL. After anesthesia, the healthy rabbit epithelium in center cornea region was removed with application of the 75% alcohol for 30 seconds. Then, the cornea was soaked in 200 μ L of type II

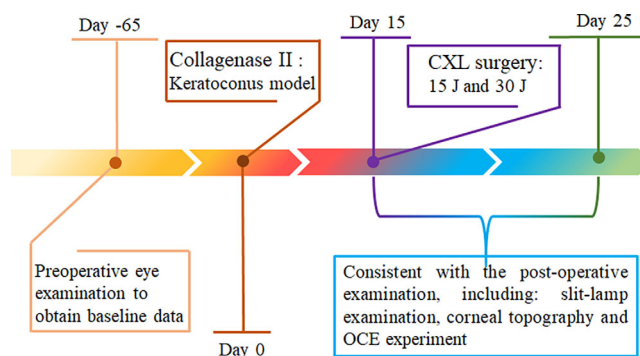


Figure 1. The timeline of the experimental procedure.

collagenase solution cornea for 30 minutes and rinsed with 0.9% sodium chloride solution to produce the keratoconus model, and a negative pressure ring is used to maintain the collagenase type II solution on the corneal surface. Intraoperative local anesthesia was performed with 5% oxybuprocaine hydrochlorate, and slit lamp and corneal topography were performed preoperatively and postoperatively. The OCE experiments were completed 2 weeks after procedure, when the inflammatory response of the cornea disappeared.

After completing the keratoconus model experiments, the keratoconus model in the first and second groups was treated with different CXL procedures without removal of the corneal epithelium: group 1 underwent CXL-15 J treatment, and group 2 underwent CXL-30 J treatment. A 9-mm diameter negative pressure retaining ring was placed in the center of the cornea. Then, transepithelial riboflavin (Ribocross IROMED Group, Rome, Italy) was dropped into the ring, followed by soaking for 15 minutes. Then, the corneal surface was rinsed with lactated Ringer's solution. A CF-X linker (IROMED Group srl) was used in pulsed mode (1 second on, 1 second off) to illuminate the central corneal region with a 4.00 mm diameter spot of 365 nm ultraviolet A at a power of 30 mW/cm². The keratoconus model of the rabbits in group 1 were irradiated with UV light for 15 minutes; then, the same riboflavin immersion step was repeated, followed by UV light irradiation for 8 minutes. The keratoconus model of the rabbits in group 2 were irradiated with UV light for 15 minutes, and then the keratoconus was soaked with riboflavin, and the treatment was repeated three times to ensure the CXL depth of the keratoconus. The OCE experiments were performed 10 days after the completion of the CXL procedure; the experimental timeline is shown in Figure 1. We repeated the data collection three times for corneal samples under each condition and calculated the average of the results.

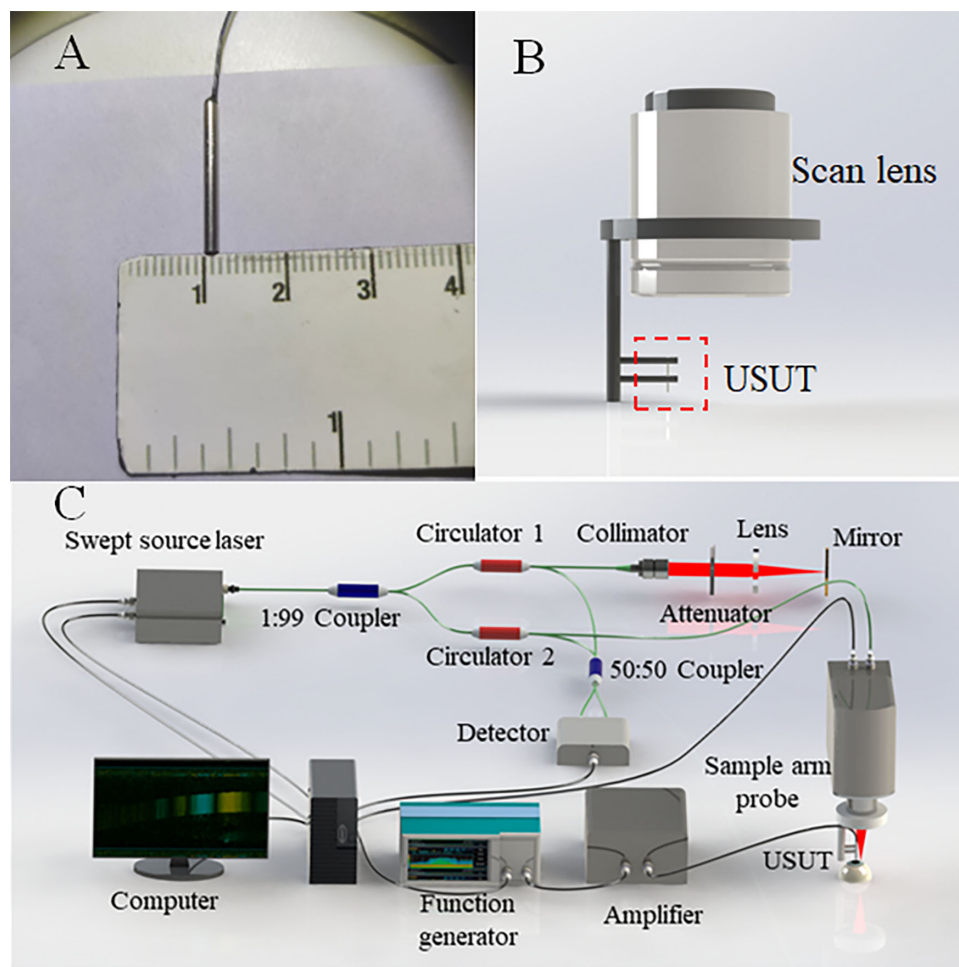


Figure 2. (A) The photograph of USUT in microscopy, the outer diameter is 1.8 mm. (B) The ARF-OCE probe diagram; USUT is marked with a red dotted box. (C) Diagram of ARF-OCE system.

ARF-OCE System Setup

A schematic diagram of the ARF-OCE system is shown in Figure 2, as reported in our previous literature,⁴³ including the acoustic radiation force (ARF) and sweep source OCT components. The ARF is generated by an USUT with an outer diameter of 1.8 mm, a focal length of 0.8 mm, and a focusing spot diameter of 1.6 mm, the photography of USUT is shown in Figure 2A. The USUT uses a single-sided meta-emission with a center frequency of 930 kHz, which is driven by a burst signal produced by a function generator and amplified by a power amplifier. The scanning objectives of the OCT system and USUT are fixed by a 3D printed holder, as shown in Figure 2B. The distance between the optical and acoustic focal lengths was determined to perform experiments. The ARF-OCE system uses a 50-kHz sweep laser with an A-line scan time of 20 μ s, a center wavelength of 1310 nm, and a bandwidth of

100 nm. The key parameters of the OCT system are an axial resolution of 5.7 μ m, a lateral resolution of 15 μ m, an signal-to-noise ratio of 105 dB, and an imaging depth of 7 mm in air, as shown in Figure 2C.

OCE Data Acquisition

A synchronization control program between the ARF and optical beam was combined with an M-B mode protocol to acquire the OCE data. For each sampling point, the M mode was repeated for a total of 500 A-line scans to detect the vibration of the corneal tissue at that point over 10 ms. The ARF was generated between the 121st and 140th A-line scans (duration of 400 μ s), which excited Lamb waves in the corneal tissue. A total of 500 sampling points were horizontally scanned, with a range of 10 mm ($\Delta x \sim 20 \mu$ m). The entire M-B mode acquisition process takes 5 seconds, and the 3D OCE data included the depth (z), transverse

width (x), and time (t), with a size of (1024, 500, and 500).

Lamb Wave Model and Data Postprocessing

For homogeneous, isotropic, elastic, and infinite-type media, the wave-based OCE method can be used to determine the relationship between Young's modulus E and the shear wave velocity c_s based on the classic physical model:

$$c_s = \sqrt{\frac{E}{2\rho(1+\nu)}}, \quad (1)$$

where ρ and ν are the density and Poisson's ratio, respectively, and ρ is 1062 kg/m³ for the cornea. However, the layered thin-plate structure of the cornea, the different media on the anterior and posterior surfaces, and the viscoelastic properties all change the boundary conditions for shear wave propagation. Therefore, other mechanical wave models, such as Lamb waves, which depend on the sample structure, have been proposed to accurately characterize the corneal biomechanics. These models differ from the shear wave velocity model because the velocity varies depending on the frequency, that is, velocity dispersion. In the wave-based OCE model, the zero-order antisymmetric Lamb wave mode is consistent with the most common mode of vibration propagation in corneal tissue, and the numerical solution can be described as^{44,45}:

$$\begin{aligned} &4k_L^3\beta_L \cosh(k_L h) \sinh(\beta_L h) - (k_s^2 - 2k_L^2)^2 \\ &\times \sinh(k_L h) \cosh(\beta_L h) \\ &- k_s^4 \cosh(k_L h) \cosh(\beta_L h) = 0 \end{aligned} \quad (2)$$

where $\beta_L = \sqrt{k_L^2 - k_s^2}$, $k_L = \frac{2\pi f}{c_L}$ is the wavenumber of the Lamb wave, f is the frequency of the Lamb wave, and c_L is the phase velocity of the Lamb wave. In addition, $k_s = 2\pi f \sqrt{\rho/U}$ is the wavenumber of the shear wave; h is the half-thickness of the cornea; and U is the viscoelasticity of the cornea. c_L can be calculated using the following equation:

$$c_L = \sqrt{\frac{2\pi \times f \times 2h \times c_s}{\sqrt{6}}}. \quad (3)$$

The temporal displacement Δd of the M-mode OCE data can be calculated as:

$$\Delta d = \frac{\lambda_0}{4\pi n} \Delta\varphi, \quad (4)$$

where λ_0 is the center wavelength of the laser, n is the refractive index of the sample, and $\Delta\varphi$ is

the optical phase change, which is obtained using the Doppler phase shift. Furthermore, the M-B mode OCE data are used to obtain the spatiotemporal displacement map (x, t) of the Lamb wave propagation at each imaging depth, and the Lamb wave group velocity is calculated by determining the propagation distance. Two-dimensional fast Fourier transform (2DFFT) of the spatiotemporal displacement maps is obtained in the wavenumber–frequency domain (k, f) to analyze the Lamb wave velocity dispersion. The distribution of the Lamb wave vibration displacement in the wavenumber–frequency domain is obtained from the 2DFFT, then the wave number corresponding to the maximum value of the spectral energy at each frequency is determined, and the phase velocity of the Lamb wave is calculated as:

$$c_L = \frac{2\pi f}{k_L}. \quad (5)$$

Then, the Young's modulus of the cornea was calculated as follows:

$$E = \frac{9\rho \times c_L^4}{(2\pi \times f \times h)^2}. \quad (6)$$

Results

Healthy Corneal Results

The 2D structural OCT image of the healthy cornea is shown in Figure 3A, and snapshots of the Lamb wave propagation after USUT excitation of the cornea are shown in Figure 3B, where the red star indicates the location of the USUT excitation. Along the depth direction, the 3D data are resliced to obtain the spatiotemporal displacement map of the Lamb wave propagation, and the spatiotemporal displacement diagram at the depth indicated by the yellow line in Figure 3A is shown in Figure 3C. The 2DFFT of the spatiotemporal displacement map of the Lamb wave is used to obtain the spectral distribution in the wavenumber–frequency domain, as shown in Figure 3D. The wavenumber value corresponding with the maximum energy at each frequency is determined, and the frequency-dependent dispersion curve of the Lamb waves is obtained according to (Equation 5), as the frequency increases the Lamb wave phase velocity will converge to a constant value, as shown in Figure 3E. The above calculation steps are repeated for the full corneal depth, and the Lamb wave phase velocity in cornea is obtained, as shown in Figure 4. The phase velocity in healthy corneal tissue gradually decreases from the anterior surface to the

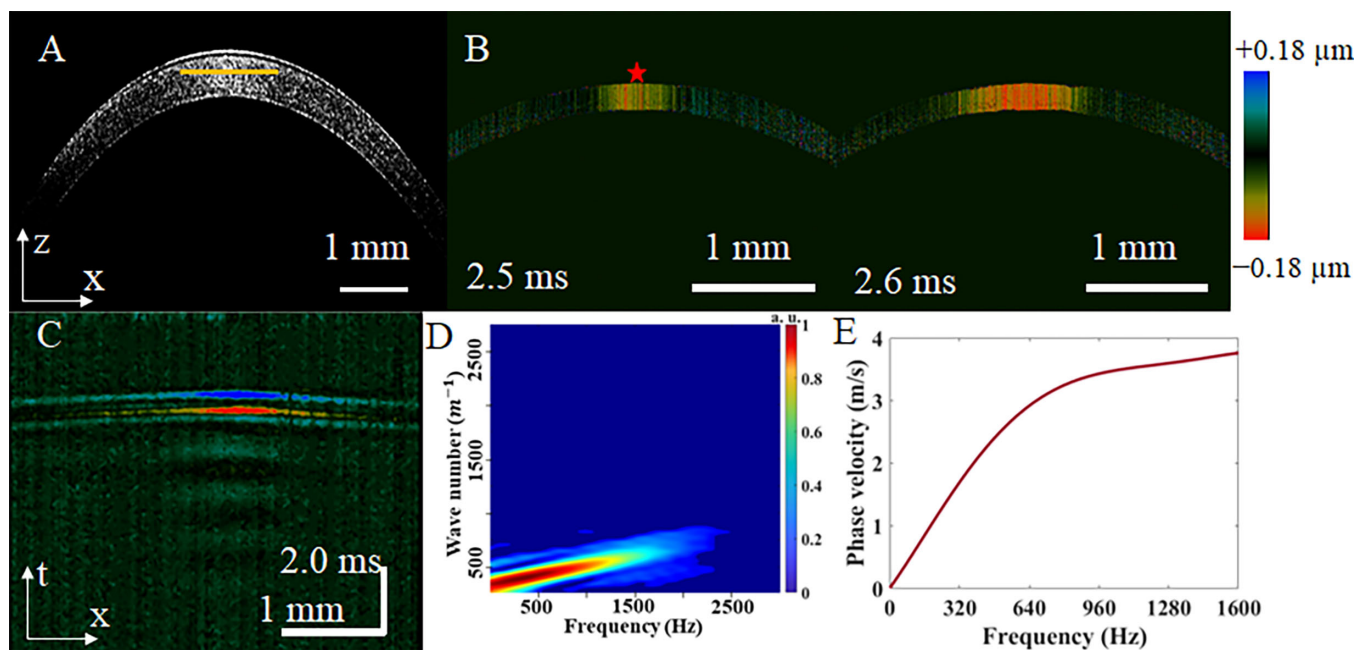


Figure 3. (A) The 2D OCT structure image. (B) The motion snapshots depiction Lamb wave propagation at different detection time, red star marked the excitation position. (C) The spatiotemporal image of the Lamb wave at the depth marked with yellow line in (A). (D) The spectrum of the Lamb wave in the wave number–frequency domain. (E) The phase velocity dispersion curve of the Lamb wave depends on the different frequency.

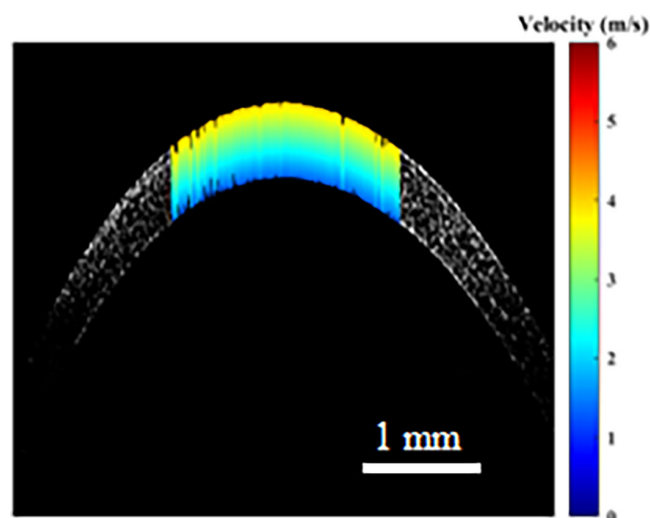


Figure 4. Depth-resolved phase velocity mapping results of the healthy cornea.

endothelium, with an average value of 3.96 ± 0.27 m/s, which is consistent with the results reported in the previous literature.^{25,38}

Keratoconus and CXL Treatment Results

After performing type II collagenase treatment on a healthy cornea to obtain a keratoconus model, the

topography results of healthy cornea and keratoconus model are shown in Figures 5A and 5B, respectively. In the keratoconus topography results, it can be observed clearly that, in the collagenase type II–treated area, there are decreased corneal thickness and significant changes in curvature compared with normal corneas.

The elastography results of keratoconus model before and after different cross-linked treatments are shown in Figure 6. A 2D structure image of the keratoconus model is shown on the left side of Figure 6A. The red box marks the area of the keratoconus lesion after collagenase II treatment, and significant defects in the epithelium and Bowman's membrane can be observed. The 2D structure images of the keratoconus model after CXL treatment at 15 J and 30 J are shown in the center and right side of Figure 6A, respectively. The treated areas are marked by blue and green boxes, respectively, and the results show that the light reflected by the cornea increases after CXL treatment. Furthermore, a snapshot of the Lamb wave vibration propagation at the same detection moment ($t = 2.2$ ms) is shown in Figure 6B. The depth-resolved results of the Lamb wave velocity for all cases obtained using the above method are shown in Figure 6C. The phase velocity of the Lamb wave was lowest in the keratoconus regions, with an average value of 3.12 ± 0.12 m/s. The corneal stiffness increased after CXL treatment, and the average phase velocity of the Lamb wave was

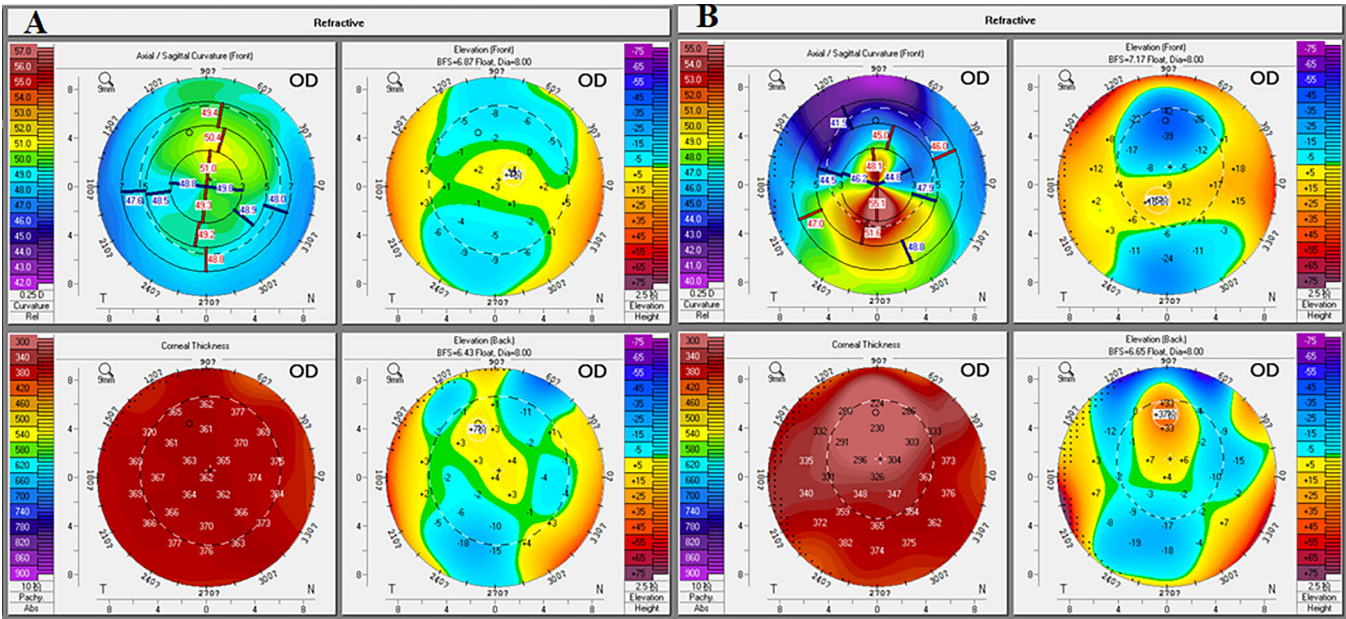


Figure 5. (A) Topography results of healthy eyes. (B) Topography results of keratoconus model.

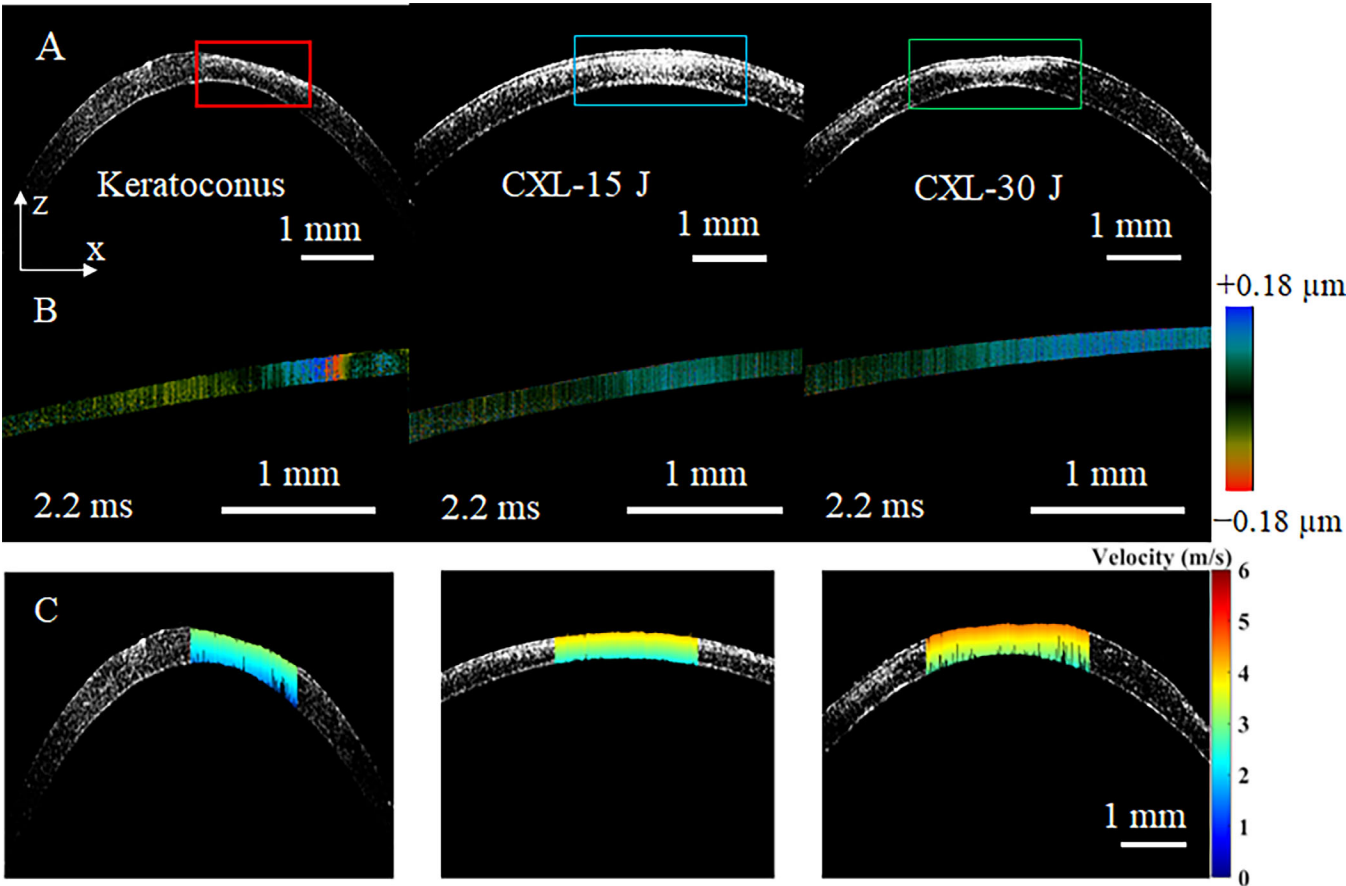


Figure 6. Keratoconus model and CXL treatment results. (A) The 2D structure images for the keratoconus model (left), CXL-15 J (center), and CXL-30 J (right). (B) The snapshot of the Lamb wave vibration propagation, the detection time $t = 2.2$ ms. (C) The depth-resolved phase velocity of the Lamb wave results.

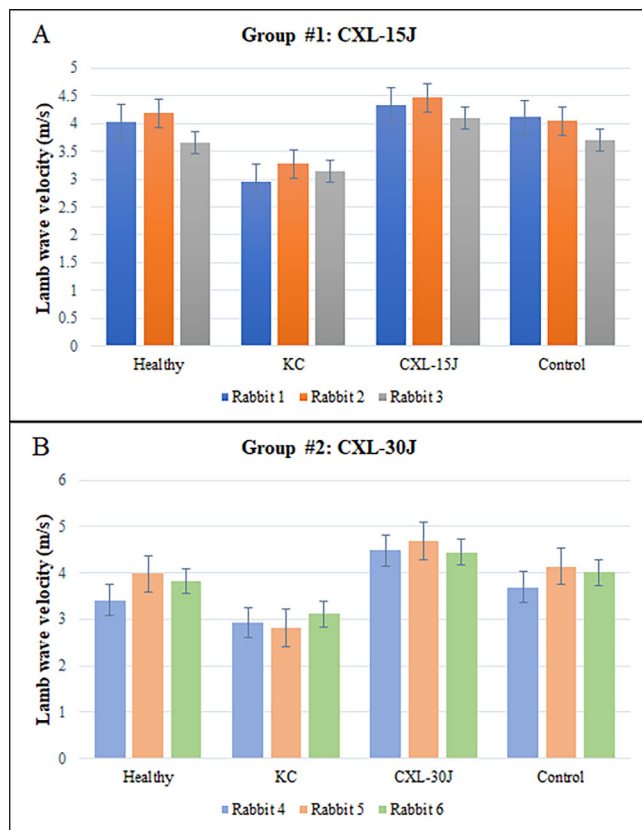


Figure 7. Statistical analysis of phase velocity in the corneas of all cases. (A) The OCE experiments results of group 1. (B) The OCE experiments results of group 2.

4.3 ± 0.19 m/s and 4.54 ± 0.13 m/s after CXL-15 J and CXL-30 J treatment, respectively. This result suggests that higher energy CXL treatment increases corneal stiffness more than lower energy CXL treatment.

Statistical Analysis Results

The phase velocities of the Lamb wave for all cases in group 1 and group 2 are shown in Figure 7. The phase velocity in each rabbit cornea is expressed as the average value, and the error bar indicates the standard deviation. The calculation procedure was as follows: for each corneal sample, we took a total of 10 phase velocities at different depth locations starting from the front surface to calculate the average velocity (in 30 μ m). The OCE experiments were also performed on the rabbit eyes without surgery, and the statistical results are presented as the control group. A Student *t* test analysis was used to compare and analysis the results of the keratoconus model and the healthy/CXL group, and a *P* value of less than 0.05 was considered significantly different. Compared with healthy corneas, the phase velocity of the Lamb wave was reduced in keratoconus regions ($P < 0.05$) and increased after 15 J CXL

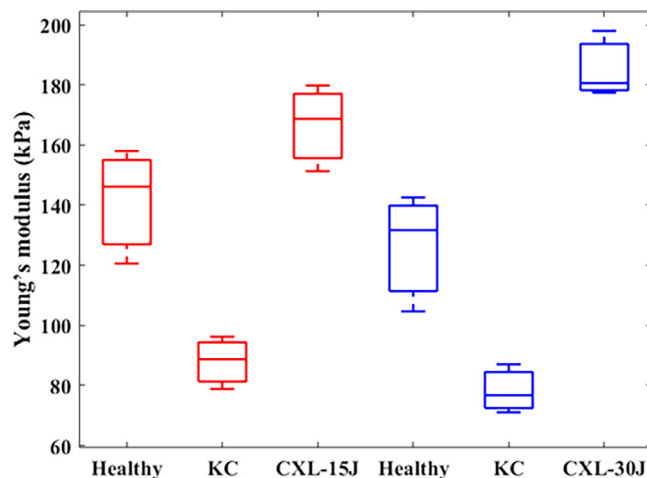


Figure 8. The statistical results of all cases Young's modulus, red on the left represents group 1, blue on the right represents group 2. The upper and lower error lines indicate the extreme values and the minimal values of the OCE experimental data, respectively. The upper and lower whiskers of the box plots contain 25% of the high and low value data, respectively.

($P < 0.05$) and 30 J CXL ($P < 0.05$). Therefore, the phase velocity was lowest in the collagenase II–treated keratoconus region, as shown in Figures 7A and 7B. For group 1 and group 2, the phase velocity was higher in the corneas after CXL treatment than in the healthy cornea and keratoconus model. Moreover, the phase velocity after CXL-30 J treatment was approximately 4.54 ± 0.13 m/s, which is higher than the phase velocity of 4.3 ± 0.19 m/s after CXL-15 J treatment ($P < 0.05$).

Moreover, the Young's modulus in all cases was calculated according to the equations (1) and (6). We selected 10 different depth locations for each corneal sample to calculate the phase velocity separately to obtain the average value of the phase velocity during data processing. Then, the corresponding corneal Young's modulus averages were calculated correspondingly. Finally, each group included three corneal samples, and the average values of Young's modulus were again calculated for healthy corneas, keratoconus, and postoperative keratoconus in each group. The statistical results of the average Young's modulus are shown in Figure 8, and the Young's modulus value of all cases as shown in Tables 1 and 2. Compared with the healthy cornea, the Young's modulus of the keratoconus model was significantly decreased (*t* test, $P = 0.039$ for group 1 and $P = 0.042$ for group 2), and the Young's modulus of the cornea after CXL treatment was significantly increased ($P = 0.01$ for CXL-15 J and $P = 0.02$ for CXL-30 J). Moreover, compared with the corneal Young's modulus after CXL-15 J treatment in group 1, the corneal Young's modulus

Table 1. The Young’s Modulus Value of All Cases in Group 1

	Healthy	KC	CXL-15J	Control
Rabbit 1	146.17	78.85	168.74	152.03
Rabbit 2	158.00	96.24	179.83	146.89
Rabbit 3	120.56	88.74	151.29	123.88
Mean ± SD	141.13 ± 19.14	87.61 ± 8.72	166.41 ± 14.39	140.42 ± 14.99

KC, keratoconus.

Table 2. The Young’s Modulus Value of All Cases in Group 2

	Healthy	KC	CXL-30J	Control
Rabbit 4	104.65	76.74	180.63	122.54
Rabbit 5	142.56	71.06	197.96	154.26
Rabbit 6	131.68	87.05	177.42	144.72
Mean ± SD	126.30 ± 19.52	78.28 ± 8.10	185.34 ± 11.05	140.51 ± 16.27

KC, keratoconus.

after CXL-30 J treatment in group 2 was increased significantly ($P = 0.04$). The results show that keratoconus have decreased stiffness, the corneal Young’s modulus increases after CXL surgery for keratoconus, and higher-energy corneal CXL surgery increases the corneal Young’s modulus more than lower-energy CXL surgery.

Discussion

In this study, we presented a novel ARF-OCE system for quantitatively evaluating corneal biomechanics of in vivo keratoconus model and keratoconus after different CXL treatments. The ARF-OCE system uses an USUT with an 0.8-mm diameter single-sided meta-emission and a 1.8-mm package diameter. A custom 3D-printed holder was used to fix the transducer to the scanning lens of the OCE system, thus decreasing the complexity of traditional OCE systems. Moreover, the Lamb wave dispersion caused by the viscoelasticity of the cornea was considered, and we obtained the dispersion curves of the Lamb wave phase velocity at different frequencies by using the 2DFFT method. Then, we performed OCE experiments and compared the Young’s modulus of healthy corneas, keratoconus model, and keratoconus after CXL surgery.

Existing clinical devices include the ocular response analyzer and the Corvis-ST, both of which can only analyze corneal biomechanics qualitatively.^{46–48} The OCE technique has been used for nondestructive, noncontact quantitative evaluation of the elastic

modulus of corneal tissue and is considered to be the elastography technique with the greatest potential for clinical translation.^{45,49,50} Conventional ARF OCE systems typically use ultrasonic transducers with centimeter-scale geometries and focused excitation to meet the requirements for optical detection.^{36,38} The ARF-OCE system proposed in this article uses an ultrasmall ultrasonic transducer with an outer diameter of 1.8 mm, a single-sided meta-emission diameter of only 0.8 mm, and a full width of height maximum of 1.6 mm in the focusing spot (Fig. 2A). The customized 3D-printed holder connects the USUT with the scanning lens of the OCE system (Fig. 2B). Thanks to its millimeter diameter, the USUT reduces OCE device complexity and facilitates integrated design, which facilitates the dynamic monitoring of changes in corneal biomechanical properties in different areas during the procedure, such as the corneal limbus. In addition, the M-B scanning algorithm combine with the Lamb wave mode enable reconstruction of the depth-resolved elastography results of the cornea.

In this experiment, an in vivo keratoconus model was obtained by treating healthy rabbit corneas with collagenase II. It has been shown that the size of the collagen layer and the number of collagen fibers in the corneal stroma are decreased in keratoconus, thus decreasing the biomechanical properties of keratoconus model; however, experimental OCE studies have lacked a suitable in vivo keratoconus model.⁵¹ Interestingly, collagenase treatment of healthy corneas with scraped epithelium degrades the collagen in the cornea, similar to keratoconus.⁴² The Bowman’s membrane in the keratoconus area was decreased after collagenase

treatment, and an irregular stroma appeared as a result of the collagen fiber breakdown caused by collagenase (Fig. 6A, left). Moreover, the thickness of the keratoconus area also decreased, as shown in Figure 5. In the ARF-OCE experiments, the amplitude of the vibration displacement produced by the ARF excitation in the corneal tissue was in the micron range, which is considered to be a small strain condition. The ARF-OCE results showed that the Young's modulus of the keratoconus model was significantly lower than that of the healthy cornea, as shown on the left side of Figure 5C and Figure 7, a finding that is consistent with the results reported in the previous literature.^{52,53} The stress-strain measurements showed a significant decrease in the stiffness of the corneas at small strains of 10% and 15% after collagenase treatment.⁴² The spatial characterization of the biomechanics of healthy cornea and keratoconus revealed that the Brillouin frequency shift was smaller in the keratoconus, which is consistent with our findings.^{31,54,55} The experimental results of this study suggest that the proposed ARF-OCE system is a powerful potential tool for screening keratoconus in clinical settings.

Furthermore, according to the clinical CXL surgery protocol, the keratoconus model was treated with different CXL energies: group 1 was treated with CXL-15 J, and group 2 was treated with CXL-30 J. The ARF-OCE system was then used to evaluate the effectiveness of different CXL surgical protocols for the treatment of keratoconus model based on the corneal biomechanical properties. Different CXL surgical protocols for OCE experiments have been reported in the literature, such as different oxygen levels, different CXL procedures.⁵⁶ In contrast with these experiments, we designed CXL protocols with different irradiation energies (CXL-15 J in group 1 and CXL-30 J in group 2) using in vivo rabbit eyes. More important, we used these two different CXL procedures to treat the keratoconus model and evaluated and compared the changes in corneal biomechanical properties using the ARF-OCE technique. The experimental results showed that both CXL procedures led to significantly increased corneal Young's moduli compared with the Young's moduli of the healthy cornea. It is worth noting that the Young's modulus of the keratoconus model after CXL-30 J treatment was significantly higher than that after CXL-15 J treatment. This result suggests that CXL procedures with different energies will have different effects on the biomechanical properties of the keratoconus model. It is important to note that, during the CXL procedure, the ambient oxygen level, riboflavin concentration, and UV radiation energy may affect the final surgical outcome, because these factors are all part of the CXL of corneal collagen fibers. Zhou et al.⁵⁶

used OCE to assess the effect of oxygen content on surgical outcomes during CXL surgery and showed that an increase or decrease in oxygen content during surgery resulted in an increase or decrease in CXL surgical efficacy, respectively. Therefore, the CXL surgical protocols should be tailored to different clinical keratoconus progressions and that the ARF-OCE technique can be used to guide the development of CXL protocols and to monitor changes in the biomechanical properties of the keratoconus during the procedure.

This work has several limitations. First, the effect of the IOP on the biomechanical properties of the cornea was not discussed. During the OCE experiments, we used a rebound tonometer to measure the IOP in the in vivo rabbit eyes in the range of 13 to 15 mm Hg, but we did not alter the IOP to assess the biomechanical properties of the keratoconus. Second, our experiment included three parts: preoperative baseline data collection, keratoconus data collection, and post-CXL surgery data collection, which lasted for a total of 3 months. Therefore, age may also be a factor affecting the biomechanical properties of the in vivo corneas. To minimize the effect of age on corneal biomechanical properties, we used the rabbit eye model aged over 5 months with more stable biomechanical properties, and an age control group should be used in future studies to accurately assess the effect of age on corneal biomechanical properties. Third, because the A-line rate of the swept-source laser is 50 kHz, each M-B scan takes a total of 5 seconds, which cannot meet the requirements of rapid 3D spatial imaging and requires the development of the higher speed lasers to be suitable for clinical testing. Finally, the corneal stromal fiber structure is changed after collagenase treatment and CXL surgery. Therefore, more accurate mathematical models are needed to characterize the corneal biomechanical properties, and the nearly incompressible transverse anisotropy model is proposed to describe the decoupled tensile and shear responses of corneal tissue.³⁹

In conclusion, we developed a novel ARF-OCE system based on the USUT to evaluate biomechanics of the in vivo healthy cornea, a keratoconus model, and keratoconus after different CXL treatments. The results showed that the Young's modulus of the keratoconus region was significantly lower than that of the healthy cornea, and the Young's modulus of keratoconus model after CXL treatment was significantly increased. Moreover, the Young's modulus of the cornea was significantly higher after CXL-30 J treatment than after CXL-15 J treatment. Thus, we have demonstrated that the ARF-OCE technique has great

potential in screening keratoconus and guiding CXL treatment in clinical settings.

Acknowledgments

Supported by the National Natural Science Foundation of China (No. 82360215), Jiangxi “Double Thousand Plan” project and the Natural Science Foundation of Jiangxi Province (No. 20212BAG70033).

Disclosure: **Y. Zhao**, None; **Y. Zhu**, None; **Y. Yan**, None; **H. Yang**, None; **J. Liu**, None; **Y. Lu**, None; **Y. Li**, None; **G. Huang**, None

* Yanzhi Zhao and Yirui Zhu contributed equally and are considered co-first authors.

References

1. Mahdaviadzad H, Bamdad S, Roustaei N, Mohaghegh S. Vision-related quality of life in Iranian patients with keratoconus: national eye institute vision function questionnaire-25. *Eye Contact Lens*. 2018;44:S350–S354.
2. Saunier V, Mercier A-E, Gaboriau T, et al. Vision-related quality of life and dependency in French keratoconus patients: impact study. *J Cataract Refract Surg*. 2017;43:1582–1590.
3. Krachmer JH, Feder RS, Belin MW. Keratoconus and related noninflammatory corneal thinning disorders. *Surv Ophthalmol*. 1984;28:293–322.
4. Rabinowitz YS. Keratoconus. *Surv Ophthalmol*. 1998;42:297–319.
5. Li Y, Meisler DM, Tang M, et al. Keratoconus diagnosis with optical coherence tomography pachymetry mapping. *Ophthalmology*. 2008;115:2159–2166.
6. Gobbe M, Guillon M. Corneal wavefront aberration measurements to detect keratoconus patients. *Contact Lens Anterior Eye*. 2005;28:57–66.
7. Sherwin T, Brookes NH. Morphological changes in keratoconus: pathology or pathogenesis. *Clin Exp Ophthalmol*. 2004;32:211–217.
8. Meek KM, Tuft SJ, Huang Y, et al. Changes in collagen orientation and distribution in keratoconus corneas. *Invest Ophthalmol Vis Sci*. 2005;46:1948–1956.
9. Klintworth GK, Damms T. Corneal dystrophies and keratoconus. *Curr Opin Ophthalmol*. 1995;6:44–56.
10. Cantemir A, Alexa AI, Galan BG, et al. Iontophoretic collagen cross-linking versus epithelium-off collagen cross-linking for early stage of progressive keratoconus—3 years follow-up study. *Acta Ophthalmol*. 2017;95:e649–e655.
11. Hayes S, Kamma-Lorger CS, Boote C, et al. The effect of riboflavin/UVA collagen cross-linking therapy on the structure and hydrodynamic behaviour of the ungulate and rabbit corneal stroma. *PLoS One*. 2013;8:e52860.
12. Wollensak G, Spoerl E, Seiler T. Riboflavin/ultraviolet-A-induced collagen crosslinking for the treatment of keratoconus. *Am J Ophthalmol*. 2003;135:620–627.
13. Schumacher S, Mrochen M, Wernli J, Bueeler M, Seiler T. Optimization model for UV-riboflavin corneal cross-linking. *Invest Ophthalmol Vis Sci*. 2012;53:762–769.
14. Raiskup F, Spoerl E. Corneal crosslinking with riboflavin and ultraviolet A1 Principles. *Ocul Surf*. 2013;11:65–74.
15. Hong J, Xu J, Wei A, et al. A new tonometer—the Corvis ST tonometer: clinical comparison with noncontact and Goldmann applanation tonometers. *Invest Ophthalmol Vis Sci*. 2013;54:659–665.
16. Luce DA. Determining in vivo biomechanical properties of the cornea with an ocular response analyzer. *J Cataract Refract Surg*. 2005;31:156–162.
17. Moshirfar M, Edmonds JN, Behunin NL, Christiansen SM. Corneal biomechanics in iatrogenic ectasia and keratoconus: a review of the literature. *Oman J Ophthalmol*. 2013;6:12.
18. Kozobolis V, Sideroudi H, Giarmoukakis A, Gkika M, Labiris G. Corneal biomechanical properties and anterior segment parameters in forme fruste keratoconus. *Eur J Ophthalmol*. 2012;22:920–930.
19. Shah S, Laiquzzaman M. Comparison of corneal biomechanics in pre and post-refractive surgery and keratoconic eyes by Ocular Response Analyser. *Contact Lens Anterior Eye*. 2009;32:129–132.
20. Ortiz D, Piñero D, Shabayek MH, Arnalich-Montiel F, Alió JL. Corneal biomechanical properties in normal, post-laser in situ keratomileusis, and keratoconic eyes. *J Cataract Refract Surg*. 2007;33:1371–1375.
21. Mercer RN, Waring IV GO, Roberts CJ, et al. Comparison of corneal deformation parameters in keratoconic and normal eyes using a non-contact tonometer with a dynamic ultra-high-speed Scheimpflug camera. *J Refract Surg*. 2017;33:625–631.

22. Hashemi H, Ambrósio R, Jr, Vinciguerra R, et al. Two-year changes in corneal stiffness parameters after accelerated corneal cross-linking. *J Biomech.* 2019;93:209–212.
23. Jędzierowska M, Koprowski R. Novel dynamic corneal response parameters in a practice use: a critical review. *Biomed Eng Online.* 2019;18:1–18.
24. Zhu Y, Zhang Y, Shi G, et al. Quantification of iris elasticity using acoustic radiation force optical coherence elastography. *Appl Optics.* 2020;59:10739–10745.
25. Zhu Y, Zhao Y, Zhang Y, et al. In vivo evaluation of the effects of SMILE with different amounts of stromal ablation on corneal biomechanics by optical coherence elastography. *Diagnostics.* 2023;13:30.
26. Qian X, Ma T, Shih C-C, et al. Ultrasonic microelastography to assess biomechanical properties of the cornea. *IEEE Trans Biomed Eng.* 2018;66:647–655.
27. Weng C-C, Chen P-Y, Chou D, Shih C-C, Huang C-C. High frequency ultrasound elastography for estimating the viscoelastic properties of the cornea using Lamb wave model. *IEEE Trans Biomed Eng.* 2020;68:2637–2644.
28. Li R, Qian X, Gong C, et al. Simultaneous assessment of the whole eye biomechanics using ultrasonic elastography. *IEEE Trans Biomed Eng.* 2023;70:1310–1317.
29. Zhang J, Murgoitio-Esandi J, Qian X, et al. High-frequency ultrasound elastography to assess the nonlinear elastic properties of the cornea and ciliary body. *IEEE Trans Ultrasonics Ferroelectrics Frequency Control.* 2022;69:2621–2629.
30. Yun SH, Chernyak D. Brillouin microscopy: assessing ocular tissue biomechanics. *Curr Opin Ophthalmol.* 2018;29:299.
31. Scarcelli G, Besner S, Pineda R, Yun SH. Biomechanical characterization of keratoconus corneas ex vivo with Brillouin microscopy. *Invest Ophthalmol Vis Sci.* 2014;55:4490–4495.
32. Scarcelli G, Kling S, Quijano E, Pineda R, Marcos S, Yun SH. Brillouin microscopy of collagen crosslinking: noncontact depth-dependent analysis of corneal elastic modulus. *Invest Ophthalmol Vis Sci.* 2013;54:1418–1425.
33. Shao P, Seiler TG, Eltony AM, et al. Effects of corneal hydration on Brillouin microscopy in vivo. *Invest Ophthalmol Vis Sci.* 2018;59:3020–3027.
34. Zhang H, Roozbahani M, Piccinini AL, et al. Depth-dependent reduction of biomechanical efficacy of contact lens-assisted corneal cross-linking analyzed by Brillouin microscopy. *J Refract Surg.* 2019;35:721–728.
35. He Y, Qu Y, Zhu J, et al. Confocal shear wave acoustic radiation force optical coherence elastography for imaging and quantification of the in vivo posterior eye. *IEEE Journal of Selected Topics in Quantum Electronics.* 2018;25:1–7.
36. Qu Y, Ma T, He Y, et al. Acoustic radiation force optical coherence elastography of corneal tissue. *IEEE Journal of Selected Topics in Quantum Electronics.* 2016;22:288–294.
37. Li Y, Zhu J, Chen JJ, et al. Simultaneously imaging and quantifying in vivo mechanical properties of crystalline lens and cornea using optical coherence elastography with acoustic radiation force excitation. *APL Photonics.* 2019;4:106104.
38. Zvietcovich F, Nair A, Ambekar YS, et al. Confocal air-coupled ultrasonic optical coherence elastography probe for quantitative biomechanics. *Optics Letters.* 2020;45:6567–6570.
39. Pitre JJ, Kirby MA, Li DS, et al. Nearly-incompressible transverse isotropy (NITI) of cornea elasticity: model and experiments with acoustic micro-tapping OCE. *Sci Rep.* 2020;10:1–14.
40. De Stefano VS, Ford MR, Seven I, Dupps WJ, Jr. Depth-dependent corneal biomechanical properties in normal and keratoconic subjects by optical coherence elastography. *Transl Vis Sci Technol.* 2020;9:4–4.
41. Zhao Y, Yang H, Li Y, et al. Quantitative assessment of biomechanical properties of the human keratoconus cornea using acoustic radiation force optical coherence elastography. *Transl Vis Sci Technol.* 2022;11:4–4.
42. Qiao J, Li H, Tang Y, et al. A rabbit model of corneal Ectasia generated by treatment with collagenase type II. *BMC Ophthalmol.* 2018;18:1–6.
43. Zhu Y, Zhao Y, Shi J, et al. Novel acoustic radiation force optical coherence elastography based on ultrasmall ultrasound transducer for biomechanics evaluation of in vivo cornea. *J Biophotonics.* 2023;16:e202300074.
44. Zvietcovich F, Pongchalee P, Meemon P, Roland JP, Parker KJ. Reverberant 3D optical coherence elastography maps the elasticity of individual corneal layers. *Nat Commun.* 2019;10:1–13.
45. Zvietcovich F, Larin KV. Wave-based optical coherence elastography: the 10-year perspective. *Prog Biomed Eng.* 2022;4:012007.
46. Ramm L, Herber R, Lorenz G, Jasper CS, Pillunat LE, Pillunat KR. Evaluation of corneal biomechanical properties using the ocular response analyzer and the dynamic Scheimpflug-Analyzer Corvis ST in high pressure and normal pres-

- sure open-angle glaucoma patients. *PLoS One*. 2023;18:e0281017.
47. Ramm L, Herber R, Spoerl E, Pillunat LE, Terai N. Measurement of corneal biomechanical properties in diabetes mellitus using the ocular response analyzer and the Corvis ST. *Cornea*. 2019;38:595–599.
 48. Shah S, Laiquzzaman M, Bhojwani R, Mantry S, Cunliffe I. Assessment of the biomechanical properties of the cornea with the ocular response analyzer in normal and keratoconic eyes. *Invest Ophthalmol Vis Sci*. 2007;48:3026–3031.
 49. Wang S, Larin KV. Optical coherence elastography for tissue characterization: a review. *J Biophotonics*. 2015;8:279–302.
 50. Larin KV, Sampson DD. Optical coherence elastography–OCT at work in tissue biomechanics. *Biomed Optic Exp*. 2017;8:1172–1202.
 51. Sawaguchi S, Yue B, Chang I, Sugar J, Robin J. Proteoglycan molecules in keratoconus corneas. *Invest Ophthalmol Vis Sci*. 1991;32:1846–1853.
 52. Santodomingo-Rubido J, Carracedo G, Suzaki A, Villa-Collar C, Vincent SJ, Wolffsohn J. Keratoconus: an updated review. *Contact Lens Anterior Eye*. 2022;45:101559.
 53. Ramier A, Eltony AM, Chen Y, et al. In vivo measurement of shear modulus of the human cornea using optical coherence elastography. *Sci Rep*. 2020;10:17366.
 54. Scarcelli G, Besner S, Pineda R, Kalout P, Yun SH. In vivo biomechanical mapping of normal and keratoconus corneas. *JAMA Ophthalmol*. 2015;133:480–482.
 55. Seiler TG, Shao P, Eltony A, Seiler T, Yun S-H. Brillouin spectroscopy of normal and keratoconus corneas. *Am J Ophthalmol*. 2019;202:118–125.
 56. Zhou Y, Wang Y, Shen M, et al. In vivo evaluation of corneal biomechanical properties by optical coherence elastography at different cross-linking irradiances. *J Biomed Optics*. 2019;24:105001–105001.